

# Josephson diode effect with Andreev and Majorana bound states

Sayan Mondal,<sup>1</sup> Pei-Hao Fu,<sup>2</sup> and Jorge Cayao<sup>1</sup>

<sup>1</sup>*Department of Physics and Astronomy, Uppsala University, Box 516, S-751 20 Uppsala, Sweden*

<sup>2</sup>*School of Physics and Materials Science, Guangzhou University, Guangzhou 510006, China*

(Dated: March 12, 2025)

Superconductor-semiconductor hybrids have been shown to be useful for realizing the Josephson diode effect, where nonreciprocity in the supercurrents occurs due to the interplay of the Josephson effect and applied magnetic fields. With the same ingredients, these Josephson junctions can also host Andreev and Majorana bound states, whose interplay with the Josephson diode effect is however not fully understood. In this work, we consider short Josephson junctions based on superconductor-semiconductor systems under homogeneous Zeeman fields and investigate the Josephson diode effect in the presence of Andreev and Majorana states. Under generic conditions, the Zeeman field component parallel to the spin-orbit axis promotes an asymmetric low-energy energy spectrum as a function of the superconducting phase, which persists in the trivial and topological phases hosting Andreev and Majorana bound states, respectively. Interestingly, this spectrum asymmetry originates supercurrents that are not odd functions of the superconducting phase difference as in common Josephson junctions, thereby developing a nonreciprocal behaviour that signals the emergence of the Josephson diode effect. We show that the Josephson diode effect is particularly promoted under the presence of both zero-energy Andreev and Majorana bound states, revealing that Josephson diodes can be realized in the trivial and topological phases of superconductor-semiconductor hybrids. We then demonstrate that the Zeeman field evolution of the diode's efficiencies is able to map the topological phase transition and the formation of Majorana bound states via an oscillatory behavior that becomes more visible in long superconductors. While Josephson diodes generally exist in the trivial and topological phases of Josephson junctions, we discover that in the tunneling regime only a Josephson diode effect in the topological phase remains due to the finite contribution of Majorana bound states. Our findings help understand the Josephson diode effect in superconductor-semiconductor hybrids and can also be useful for guiding the realization of Majorana-only Josephson diodes as well as for identifying Majorana states.

## I. INTRODUCTION

Josephson junctions (JJs) have been one of the most studied systems in condensed matter physics not only because they can host novel physics but also due to their promising applications [1–10]. JJs composed of two coupled superconductors enable the flow of a dissipationless supercurrent known as the Josephson effect [1], which is carried by Andreev bound states due to a finite phase difference between superconducting order parameters [4, 11–20]. The Josephson effect (JE) and Andreev bound states (ABSs) in JJs have been shown to be crucial for superconducting qubits [21–28], superconducting spintronics [29–34], superconducting quantum interference devices [35–40], and, more recently, also for realizing Josephson diodes [41–47]. In this regard, Josephson diodes (JDs) are of particular relevance because they result from nonreciprocal supercurrents [41–86], which makes them useful for dissipationless, or low-dissipation, circuit elements in superconducting devices [87–93]. JDs can thus pave the way for transformative advancements in electronic device technologies [47, 94–97].

It is by now understood that the necessary conditions for realizing JDs involve breaking time-reversal and inversion symmetries [45, 65, 98–101]. While these requirements can be achieved in distinct setups [10, 47], superconductor-semiconductor hybrids under magnetic fields have attracted considerable attention [42, 43, 45, 46, 58, 60, 61, 72–86, 100] due to their promising

properties and great experimental and theoretical advances [102–111]. In fact, JJs based on superconductor-semiconductor hybrids are predicted to host a topological phase characterized by the emergence of four Majorana bound states (MBSs) at large Zeeman fields [112–121], in addition to the ABSs present in the trivial phase [14, 19, 20, 122–125]; see also Refs. [102–111]. While JDs have been widely studied in the trivial phase with ABSs, not many studies addressed JDs with MBSs. In particular, there exist limited works addressing JDs with four MBSs in superconductor-semiconductor hybrids [73, 81], where they consider transparent JJs with an inhomogeneous magnetic field that does not affect the topological protection of MBSs but is rather challenging to achieve. In this regard, the effect of MBSs on the efficiency of JDs when the topological protection is reduced as well as the possibility to promote JDs only with MBSs remain to be addressed.

In this work, we consider JJs with Rashba spin-orbit coupling (SOC), which can be realized in superconductor-semiconductor hybrids, and investigate the emergence of JDs when homogeneous magnetic fields are applied. We find that, when the Zeeman field has a component parallel to the SOC, the Andreev spectrum is asymmetric with respect to the superconducting phase difference, including regimes with ABSs and MBSs in the trivial and topological phases of transparent JJs, respectively. We then demonstrate that this asymmetry induces current-phase curves possessing distinct positive and negative

critical currents which gives rise to nonreciprocal Josephson transport and to JDs. We obtain that, while the efficiency of the JDs is largest in the trivial regime of transparent JJs, the lower efficiencies of JDs in the topological phase trace the topological phase transition and the formation of MBSs. These signatures can be proved by the Zeeman dependence of the diode's efficiencies, which develop a kink at the topological phase transition and an oscillatory pattern uniquely associated to the spatial nonlocality of MBSs. By increasing the length of the superconductors, the efficiency of the JDs in the topological phase reaches higher values and its oscillations develop short periodicity as a response to MBSs becoming more zero energy and spatially nonlocal. We further discover that, while JDs emerge in the presence of ABSs and MBSs in transparent JJs, by reducing the junction's transmission, it is possible to lower the diode's efficiency in the trivial regime such that JDs only emerge in the topological phase with MBSs. These results therefore provide fundamental understanding of JDs in semiconductor-based JJs with Andreev and Majorana states.

This paper is organized as follows: In Sec. II, we describe the Hamiltonian of the JJ and its band structure. Sec. III explores the phase- and Zeeman-field-dependent ABSs and MBSs. In Sec. IV, we analyze the asymmetric Josephson current across the JJ. The emergence of the JD is discussed in Sec. V by examining the critical current and efficiency as a function of the Zeeman field. Finally, in Sec. VI, we summarize our findings. In Appendix A, we have presented the robustness of JD's efficiency in presence of a finite temperature.

## II. THE JOSEPHSON JUNCTION MODEL

We consider a JJ based on a single-channel semiconducting nanowire with proximity induced superconductivity and an homogeneous magnetic field, see Fig. 1(a). In momentum space, we model the semiconductor with proximity-induced superconductivity by a Bogoliubov-de Gennes (BdG) Hamiltonian that reads [126–129]

$$H_{\text{BdG}} = \left( -\frac{\hbar^2 \partial_x^2}{2m^*} - \mu \right) \tau_z \sigma_0 - i\alpha_R \tau_z \sigma_y \partial_x + B_x \tau_z \sigma_x + B_y \tau_0 \sigma_y + \Delta \tau_y \sigma_y, \quad (1)$$

where  $m^*$  represents the electron's effective mass and  $\mu$  the chemical potential measured from the bottom of the band. The second term describes the Rashba SOC with SO axis along  $y$  and  $\alpha_R$  being the strength of the coupling. The applied magnetic field induces a homogeneous Zeeman field  $\mathbf{B}$  forming an angle  $\theta$  with the  $x$ -axis, such that  $B_x = B \cos \theta$  (the third term) and  $B_y = B \sin \theta$  (the fourth term) are components perpendicular and parallel to the SO axis, respectively; see Fig. 1(a). The fifth term represents the proximity induced superconductivity, with  $\Delta$  being the induced spin-singlet  $s$ -wave pair potential. The  $i$ -th Pauli matrices  $\sigma_i$  and  $\tau_i$ , with  $i = x, y, z$ , operate in the electron's spin and particle-hole subspaces,

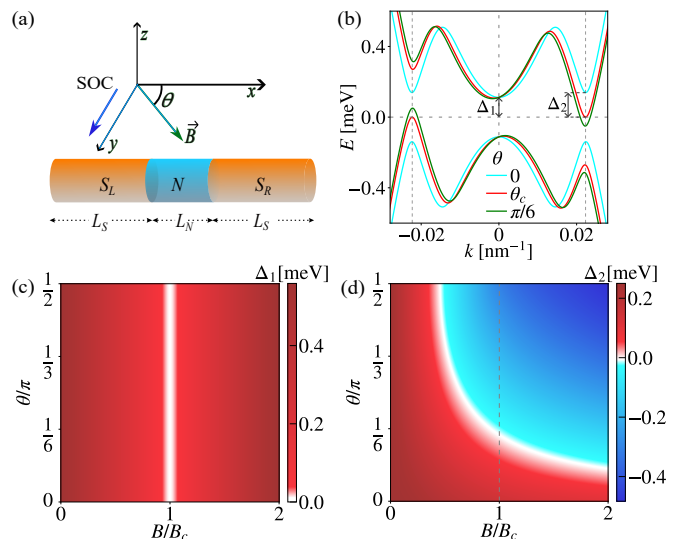


FIG. 1. (a) A JJ formed by a nanowire with SOC and an homogeneous magnetic field. The left and right sides of the nanowire denoted by  $S_{L,R}$  (orange regions) are of finite length and contain proximity induced superconductivity from conventional superconductors, while the finite middle light blue region is left without superconductivity and denoted by  $N$ . The JJ is formed along  $x$ , while the SO axis lies along the  $y$ -direction and is indicated by the blue arrow. The Zeeman field  $B$  results from an applied magnetic field throughout the JJ and makes an angle  $\theta$  with the  $x$ -axis, thus containing components that are parallel and perpendicular to the SO axis. (b) Energy versus momentum for distinct values of  $\theta$ , indicating the two gaps  $\Delta_{1(2)}$  at zero momentum (positive Fermi momenta). Here, the Zeeman field magnitude is  $B = 1.2B_c$ , for which  $\Delta_2 = 0$  at  $\theta_c \approx 0.1216\pi$  indicated by red curve. (c,d) Gaps  $\Delta_{1,2}$  as a function of  $\theta$  and  $B$ , with  $\Delta_2$  found at  $+k_F$  with respect to the Fermi level. Here,  $B = B_c$  marks the topological phase transition where  $\Delta_1 = 0$ . Parameters:  $\alpha_R = 20\text{meVnm}$ ,  $\Delta = 0.25\text{meV}$ , and  $\mu = 0.5\text{meV}$ .

respectively, while  $\sigma_0$  and  $\tau_0$  denote the identity matrices in these spaces.

To understand the role of the Zeeman field, we diagonalize Eq. (1) and in Fig. 1(b) we show the energy versus momentum at distinct values of the angle  $\theta$  at fixed Zeeman field amplitude  $B = 1.2B_c$ , where  $B_c = \sqrt{\mu^2 + \Delta^2}$  and its physical meaning is discussed below. At  $\theta = 0$ , there only exists a Zeeman field component perpendicular to the SO axis; the energy versus momentum in this case exhibits two distinct gaps at low momentum and at the Fermi momenta  $\pm k_F$ , here denoted as  $\Delta_1$  and  $\Delta_2$  for zero momentum and  $+k_F$ , respectively, see cyan curve in Fig. 1(b). As  $\theta$  takes finite values, there appears a finite component  $B_y$  parallel to the SO axis; the energy versus momentum gets tilted, maintaining constant  $\Delta_1$  but decreasing  $\Delta_2$  at  $+k_F$ , see red and green curves in Fig. 1(b). When  $\Delta = B_y$ , the outer gap vanishes ( $\Delta_2 = 0$ ) at a critical angle determined by  $\theta_c = \arcsin(\Delta/B)$  [130], see red curve in Fig. 1(b); for our parameters, the critical angle is  $\theta_c \approx 0.1216\pi$ . When varying the magnitude of

the Zeeman field  $B$ , both the inner and outer gaps ( $\Delta_1$  and  $\Delta_2$ ), exhibit a strong dependence. This can be seen in Fig. 1(c,d), where we show  $\Delta_{1,2}$  as a function of  $B$  and  $\theta$ . We restrict  $\theta$  to the range 0 and  $\pi/2$  because for  $\pi/2 < \theta < \pi$  region,  $\Delta_2$  follows the same evolution but in reverse;  $\Delta_2$  returns to its initial values at  $n\pi \pm \theta$  for  $n \in \mathbb{Z}$ . In this scenario, the inner gap  $\Delta_1$  vanishes at  $B = B_c$ , a situation that is insensitive to variations of  $\theta$  and corresponds to the topological phase transition separating the trivial and topological phases for ( $B < B_c$ ) and ( $B > B_c$ ), respectively; see white region in Fig. 1(c). In the topological phase, topologically protected MBSs emerge at zero energy separated from the quasicontinuum by  $\Delta_2$  and located at the ends of the system with a localization length defined by  $\sim 1/\Delta_2$  [111]. Moreover, as already anticipated in Fig. 1(b), the outer gap  $\Delta_2$  decreases as  $\theta$  takes finite values and vanishes at the critical angle that depends on  $B$  at fixed  $\Delta$ , see white region in Fig. 1(d) where the red and blue colors indicate that the outer gap takes positive ( $\Delta_2 > 0$ ) and negative ( $\Delta_2 < 0$ ) values. The reduction of  $\Delta_2$  suggests that the topological protection of localization of MBSs is affected by the Zeeman field parallel to the SO axis. Despite the apparent detrimental effect of the parallel Zeeman field  $B_y$ , we will show below that it plays an important role for realizing the JD effect. In fact, from a symmetry perspective, the Rashba term breaks the inversion symmetry, while the Zeeman terms break the time-reversal symmetry. Notably, the Zeeman field component  $B_y$  also breaks the  $x$ -inverting symmetry and, as we will see below, is responsible for inducing the JD effect [100].

To study the JD effect in JJs formed by single-channel semiconducting nanowires, we discretize Eq. (1) into a tight-binding lattice with a lattice constant  $a = 10$  nm divided into three regions of finite length, as sketched in Fig. 1(a). The central region (denoted by N) has no superconductivity ( $\Delta = 0$ ), while the left and right regions (denoted by  $S_{L/R}$ ) have proximity-induced superconductivity characterized by  $\Delta e^{\pm i\phi/2}$ ; here  $\Delta$  is the spin-singlet  $s$ -wave pair potential and  $\pm\phi/2$  are the superconducting phases that lead to a finite phase difference across the junction and enable the study of the Josephson effect [111, 117]. The normal and superconducting regions have lengths  $L_N$  and  $L_S$ . Thus, the JJ is described by a Nambu Hamiltonian written as

$$H_{\text{SNS}} = \begin{pmatrix} h_{\text{SNS}} & \Delta(x) \\ \Delta^\dagger(x) & -h_{\text{SNS}}^* \end{pmatrix} \quad (2)$$

where

$$\Delta(x) = \begin{pmatrix} \Delta_{S_L} & 0 & 0 \\ 0 & 0 & 0 \\ 0 & 0 & \Delta_{S_R} \end{pmatrix}, \quad (3)$$

with  $\Delta_{S_R} = \Delta e^{i\phi/2} \sigma_y$  and  $\Delta_{S_L} = \Delta e^{-i\phi/2} \sigma_y$ , and

$$h_{\text{SNS}} = \begin{pmatrix} H_{S_L} & H_{S_L N} & 0 \\ H_{S_L N}^\dagger & H_N & H_{N S_R} \\ 0 & H_{N S_R}^\dagger & H_{S_R} \end{pmatrix}. \quad (4)$$

The diagonal elements of  $h_{\text{SNS}}$  in Eq. (4) denoted by  $H_\alpha = H_0$ , with  $\alpha = N, S_{L,R}$ , take the following form

$$H_0 = \sum_n c_n^\dagger h_{nn} c_n + \sum_{\langle n,m \rangle} c_n^\dagger V_{nm} c_m + \text{h.c.}, \quad (5)$$

where  $c_n^\dagger$  ( $c_n$ ) is the creation (annihilation) operator at the  $n$ -th site involving spin up and down, while  $h$  represents onsite energies and  $V$  characterizes nearest neighbor hopping terms with the sum label  $\langle i,j \rangle$  also indicating hopping between nearest neighbor sites. Here, the onsite ( $h_{nn}$ ) and hopping ( $V_{nm}$ ) matrices are given by

$$\begin{aligned} h_{nn} &= (2t - \mu_n) \sigma_0 + B_x \sigma_x + B_y \sigma_y, \\ V_{nm} &= -t \sigma_0 + i t_{\text{SO}} \sigma_y, \end{aligned} \quad (6)$$

where  $t = \hbar^2/(2m^* a^2)$  is the hopping,  $t_{\text{SO}} = \alpha_R/(2a)$  is the Rashba SOC hopping, and  $\mu_i$  is the chemical potential which we keep equal in all the regions unless otherwise stated. Furthermore, we note that the matrices  $H_{S_{L(R)}N}$  in Eq. (4) couple the  $S_{L,R}$  and N regions and hence contain finite entries only for the adjacent sites that are located at the interfaces between the  $S_{L,R}$  and N regions; they are thus determined by  $V_{nm}$ . We note that the normal transmission across the JJ can be controlled by the hopping parameter that enters into the  $H_{S_{L(R)}N}$  matrices, which here we denote as  $\bar{V}_{nm} \rightarrow \tau V_{nm}$  with  $\tau \in [0, 1]$ . Thus,  $\tau = 1$  describes fully transparent JJs, while  $\tau \ll 1$  models JJs in the tunneling regime. In our simulations, we use realistic parameters such as the electron effective mass  $m^* = 0.015 m_e$ , the strength of Rashba SOC  $\alpha_R = 20$  meV-nm, and superconducting gap  $\Delta = 0.25$  meV, within the range of experimental values given for InSb or InAs semiconductors and Al or Nb superconductors, see e. g., Ref. [105]. Additionally, we fix the chemical potential at  $\mu = 0.5$  meV. Thus, taking into account these realistic parameters, we next model JJs and explore the formation of ABSs and MBSs in the low energy spectrum and identify under which conditions a JD effect emerges.

### III. LOW-ENERGY SPECTRUM: EMERGENCE OF ANDREEV AND MAJORANA STATES

We start by analyzing the low-energy spectrum of the JJ modelled by Eq. (2), taking into account a short junction with  $L_N = 20$  nm and  $L_S = 2$   $\mu\text{m}$ . The motivation to choose a short junction relies on that, in this regime, only a few ingap states appear within the superconducting gap, as we see next. In Fig. 2 we present the low-energy spectrum as a function of the superconducting phase difference  $\phi$  in the trivial and topological phases for distinct  $\theta$ ; the energy levels within the induced gap are indicated by red color, while the gaps  $\Delta_{1(2)}$  discussed in previous section are marked by brown (magenta) horizontal lines. The first observation is that the spectrum develops a strong dependence on  $\phi$  and exhibits several

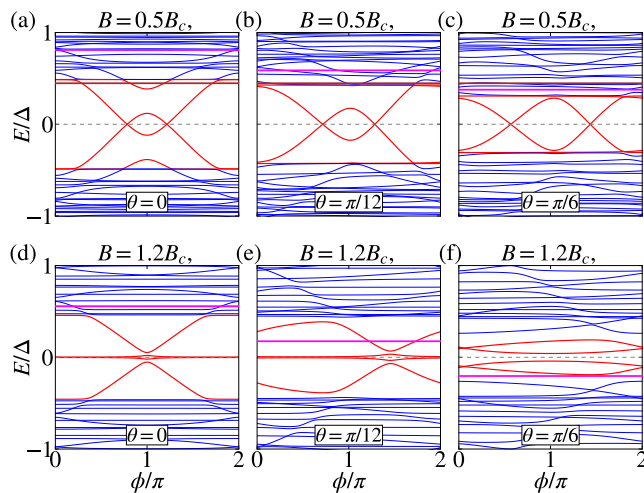


FIG. 2. (a-f) Low-energy spectrum as a function of the superconducting phase difference  $\phi$  in the trivial (a-c) and topological phases (d-f) at distinct values of  $\theta$ . The four energy levels closest to zero energy  $E = 0$  are indicated in red color. The brown and magenta horizontal lines represent the inner ( $\Delta_1$ ) and outer ( $\Delta_2$ ) gaps, respectively, obtained from the bulk model given by Eq. (1). In the bottom panels  $\Delta_1$ , appears at higher energies, that is,  $\Delta_1 > \Delta$ .  $\Delta_2$  in (f) lies below  $E = 0$ . Parameters:  $L_S = 2 \mu\text{m}$  and  $L_N = 20 \text{ nm}$ ,  $\tau = 1$ , while the rest of parameters are the same as in Fig. 1.

interesting features depending on the value of  $\theta$ . When  $\theta = 0$ , the Zeeman field is oriented perpendicular to the SO axis and the phase-dependent energy spectrum exhibits a symmetric profile with respect to  $\phi = \pi$ . In this case, the spectrum in the trivial phase ( $B < B_c$ ) hosts one pair of ABSs at finite  $B$  which develops zero energy crossings around  $\phi = \pi$  as a result of SOC, see Fig. 2(a) and also Refs. [14, 19]. In the topological phase ( $B > B_c$ ) shown in Fig. 2(d), the ingap ABSs are topological and define the formation of four MBSs: at  $\phi = 0$ , the lowest almost dispersionless energy levels define a pair of MBSs located at the outer ends of the left and right superconductors, while at  $\phi = \pi$  the system hosts two additional MBSs at the inner sides of the junction, making a total of four MBSs [112, 115, 117]. Due to the finite length of superconductors, the four MBSs develop a finite energy splitting at  $\phi = \pi$ , which becomes zero when the length of the superconductors is larger than twice the Majorana localization length [115]. The dependence of this energy splitting is thus a direct result of MBSs being located at the system's ends and, hence, a property tied to the inherent Majorana nonlocality [118, 120, 131, 132]. The trivial phase does not exhibit a dependence on the length of the superconductors because it does not host nonlocal quasiparticles [118, 120, 121, 132].

When  $\theta \neq 0$ , the Zeeman field acquires a nonzero component parallel to the SO axis  $B_y$ , which then gives rise to a phase-dependent low-energy spectrum that is asymmetric with respect to  $\phi = \pi$  in the trivial and topological phases, see Fig. 2(b,c,e,f). This asymmetry becomes

more pronounced as  $\theta$  (or equivalently  $B_y$ ) increases, impacting both the in-gap energy levels and the quasicontinuum above the induced superconducting gap. In the trivial phase ( $B < B_c$ ), the asymmetry in the ABSs is weak, but, as  $\theta$  increases, the induced superconducting gap  $\Delta_2$  (magenta line) reduces and the zero-energy crossings happen further away from  $\phi = \pi$ , see Fig. 2(b,c). Interestingly, in the topological phase ( $B > B_c$ ) MBSs exhibit a much stronger asymmetry when  $\theta \neq 0$  in comparison to the trivial regime, see Fig. 2(e,f). A notable effect of  $\theta \neq 0$  is that the zero-energy splitting of MBSs can occur at phase values other than  $\phi = \pi$ , as shown in Fig. 2(d,e,f), thus unveiling the crucial role of the Zeeman field parallel to the SO axis. Another effect of  $\theta \neq 0$  in the topological phase, already seen in Fig. 1(b) of the previous section, is that the gap  $\Delta_2$  reduces and can even become negative, see magenta line in Fig. 2(e,f). This implies that levels from the quasicontinuum lower their energies and can coexist with MBSs [Fig. 2(e,f)], thus damaging the topological protection of MBSs provided by  $\Delta_2$ . Yet another impact of  $\theta \neq 0$  is that even the zero-energy splitting at phases other than  $\phi = \pi$  are not apparent anymore, with the outer MBS even acquiring finite energies for all phases, see Fig. 2(f) when  $\Delta_2$  is negative. Despite all the noted effects of  $\theta \neq 0$ , and hence of the Zeeman field component parallel to the SO axis, we will see later that the asymmetry in the phase-dependent spectrum with respect to  $\phi = \pi$  is perhaps the most important as it gives rise to the JD effect.

Having understood the phase-dependent energy spectrum, we now analyze the energy spectrum as a function of the Zeeman field, presented in Fig. 3 at fixed  $\phi$  and  $\theta$ . The values of  $\theta$  correspond to the chosen ones in Fig. 2, while the values of  $\phi = 0$  and also  $\phi$  at which the four MBSs develop the zero-energy splitting. At  $B = 0$ , the superconducting pair potential produces a gap in the spectrum irrespective of the value of  $\theta$ , see Fig. 3(a-c). Here,  $\theta$  affects the ingap ABSs appearing at  $B = 0$  for  $\phi$  other than  $\phi = 0$ , forcing them to even acquire higher (lower) energies, see Fig. 3(d-f). As  $B$  takes finite values, the gap in the spectrum reduces and eventually closes at the topological phase transition marked by  $B = B_c$ , which is independent of the value of  $\theta$  [Fig. 3]; the closing of the energy gap closely follows the closing of the bulk gap  $\Delta_1$ , depicted by brown curve in Fig. 3. As the system transitions into the topological phase  $B > B_c$  at  $\theta = 0$ , the energy gap reopens and leaves two (four) energy levels oscillating around zero energy as  $B$  further increases at  $\phi = 0$  ( $\phi = \pi$ ), see Fig. 3(a,d); these energy levels define the two MBSs at  $\phi = 0$  (four MBSs at  $\phi$ ) discussed in Fig. 2(d) and are within the topological gap  $\Delta_2$  shown by magenta curve. A finite  $\theta$  in the topological phase has a huge impact on the low-energy spectrum, with the most immediate feature being the proliferation of ingap states coming from the quasicontinuum at energies close to those of MBSs, see Fig. 3(b,c,e,f). Even more dramatically is that the low-energy spectrum in the topological phase can be even gapless at certain values

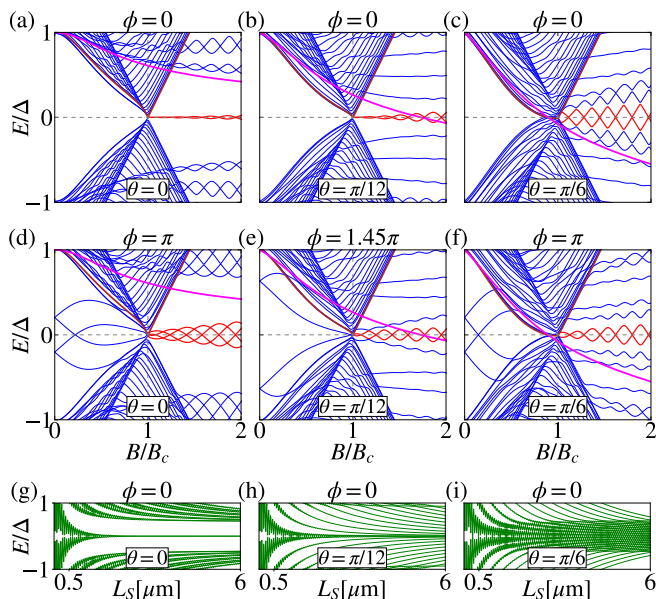


FIG. 3. (a-f) Low-energy spectrum as a function of the magnitude of the Zeeman field  $B$  for distinct values of  $\theta$  at  $\phi = 0$  (a-c) and  $\phi \neq 0$  (d-f). The choice of  $\phi \neq 0$  in (d-f) corresponds to  $\phi$  where the four MBSs split in energy, see Fig. 2(d-f). In (f),  $\phi = \pi$  is selected since the exact splitting point of the MBSs is unclear, see Fig. 2(f). The brown and magenta curves show the Zeeman dependence of  $\Delta_1$  and  $\Delta_2$ , respectively. (g-i) illustrate the dependence of the low-energy spectra on  $L_S$ , with  $B = 1.8B_c$ . Parameters:  $L_S = 2 \mu\text{m}$  and  $L_N = 20 \text{nm}$ ,  $\tau = 1$ , while the rest of parameters are the same as in Fig. 1.

of  $\theta$  [Fig. 3(c,f)]; the vanishing of the topological gap becomes more evident in JJs with long superconductors  $L_S$  [Fig. 3(g-i)]. The loss of the energy gap in the topological phase is consistent with the behaviour of the bulk gap at the positive Fermi point  $\Delta_2$ , which, for certain  $\theta$ , can vanish either in the topological phase [Fig. 3(b,e)] or in the trivial phase [Fig. 3(c,f)]. Thus, Zeeman fields with a finite component parallel to the SO axis via  $\theta \neq 0$  deteriorate the topological gap that protects MBSs from higher energy states. Despite these seemingly negative effects, we will see in the next sections that  $\theta \neq 0$  promotes nonreciprocal Josephson transport and hence a JD effect.

#### IV. NON-RECIPROCAL PHASE-DEPENDENT JOSEPHSON CURRENTS

In this section, we investigate the impact of the Zeeman field oriented at specific angles relative to the SO axis on the supercurrents across short JJs modelled by Eq. (2). At finite temperatures, the Josephson current can be obtained from the phase-dependent discrete energy spectrum as [14]

$$I(\phi) = -\frac{e}{\hbar} \sum_{\varepsilon_n > 0} \tanh\left[\frac{\varepsilon_n}{2\kappa_B T}\right] \frac{d\varepsilon_n(\phi)}{d\phi}, \quad (7)$$

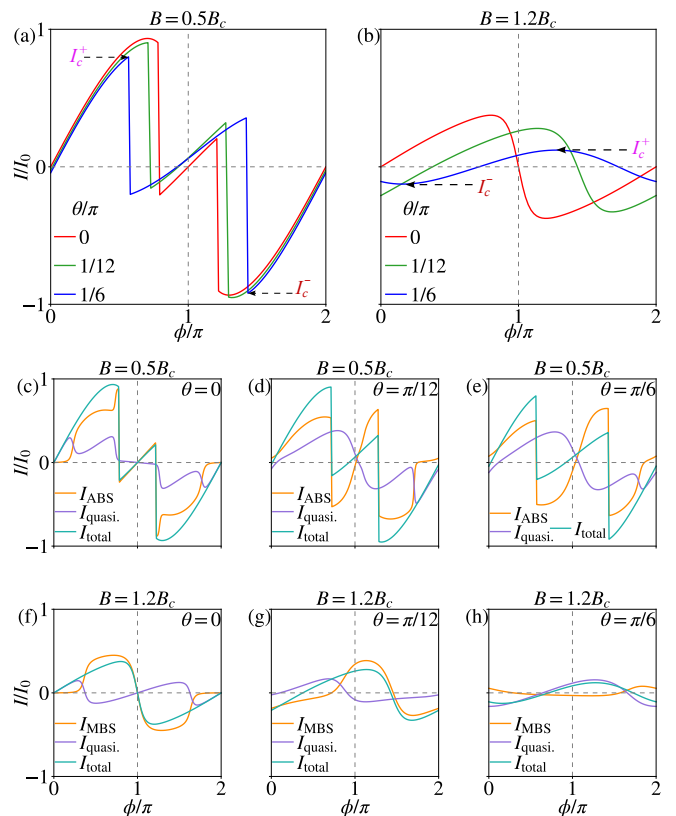


FIG. 4. (a,b) Josephson currents as a function of the superconducting phase difference  $I(\phi)$  in the trivial (a) and topological (b) phases for distinct  $\theta$ . The Josephson currents in (a,b) correspond to the phase-dependent spectrum shown in Fig. 2. (c,d) Contribution of the ingap states ( $I_{\text{ingap}}$ ) and quasiconductum ( $I_{\text{quasi.}}$ ) to the total Josephson current  $I(\phi)$  corresponding to (a) in the trivial phase. (e,f) The same as in (c,d) but corresponding to (b) in the topological phase. Parameters:  $L_S = 2 \mu\text{m}$  and  $L_N = 20 \text{nm}$ ,  $\tau = 1$ ,  $I_0 = e\Delta/2\hbar$ ,  $T = 0$ , while the rest of parameters are the same as in Fig. 2.

where  $\varepsilon_n(\phi)$  denotes the discrete positive phase-dependent energy levels,  $\kappa_B$  is the Boltzmann constant, and  $T$  the temperature. While we primarily focus on the zero-temperature limit ( $T = 0$ ), the results that we present here remain robust at finite temperatures but smaller than  $\Delta$ , see Appendix A. We then numerically calculate the Josephson current  $I(\phi)$  for distinct  $\theta$  across a transparent JJ and present it in Fig. 4 in the trivial and topological phases. In the trivial phase at  $\theta = 0$ , the supercurrent  $I(\phi)$  has a regular behavior, where  $I(\phi) = -I(-\phi)$  and  $I(\phi) = 0$  at  $\phi = m\pi$ , with  $m \in \mathbb{Z}$ , and developing a sawtooth-like profile at phases around  $\phi = \pi$  coming from the SOC effect in the spectrum, see red curve in Fig. 4(a). With the introduction of  $\theta \neq 0$ , and hence of  $B_y$  parallel to the SO axis, the Josephson current  $I(\phi)$  becomes asymmetric with respect to  $\phi = \pi$  [Fig. 4(a)], which is a consequence of the asymmetric phase dependent Andreev spectrum shown in Fig. 2(a-c). Another consequence is that, at finite  $\theta$ , the supercurrent develops distinct global maximum and

minimum  $I_c^\pm = \max_\phi[\pm I(\phi)]$ , leading to  $I(\phi) \neq -I(-\phi)$  as with  $\theta = 0$ . We note that  $I_c^\pm$  are known as critical currents. The profile of  $I(\phi)$  is largely determined by the ingap ABSs, although a finite contribution exist due to the quasicontinuum, see Fig. 4(c,d,e). In the topological regime, the effect of  $\theta \neq 0$  remains in the Josephson current, inducing an asymmetric profile with respect to  $\phi = \pi$  due to the phase-dependent energy spectrum and different values of the global maximum and minimum  $I_c^\pm$ , see Fig. 4(b). The regular properties of  $I(\phi)$  with MBSs at  $\theta = 0$ , including the sine-like profile with  $\phi$  and  $I(\phi) = 0$  for  $\phi = m\pi$ , are considerably affected in the topological phase when  $\theta \neq 0$ , leading to a  $\phi_0$ -junction behavior that is more pronounced than in the trivial phase. The global maximum and minimum  $I_c^\pm$  in the topological phase are in general smaller than in the trivial phase but are more susceptible to changes in  $B$  and  $\theta$  [Fig. 4(a,b)]; hence, the values of  $\phi$  at which  $I_c^\pm$  occur in the topological phase, denoted as  $\phi_\pm$ , vary more with both  $B$  and  $\theta$ . For instance, for  $B = 1.2B_c$ ,  $\phi_+$  shifts from  $\phi < \pi$  at  $\theta = 0$  to  $\phi > \pi$  at  $\theta = \pi/12$ . This shift in  $\phi_\pm$  correlates with the zero-energy states found in Fig. 2 and Fig. 3. Moreover, we note that in the topological phase, the contribution to  $I(\phi)$  is largely dominated by the MBSs even for  $\theta \neq 0$ , but when the topological gap is vanishingly small, the quasicontinuum develops a considerable contribution, Fig. 4(f,g,h).

Before going further, we highlight that, although  $\theta \neq 0$  has multiple consequences on  $I(\phi)$ , the behaviour of  $I(\phi)$  exhibiting  $I_c^+ \neq I_c^-$  at  $\theta \neq 0$  implies that there emerges a non-reciprocal Josephson transport across the JJs considered here. Notably, this nonreciprocal transport behavior signals the emergence of the JD effect, entirely due to  $\theta \neq 0$  which corresponds to the presence of a Zeeman field component parallel to the SOC. Thus, the considered JJs exhibit a JD effect in the trivial and topological phases with ABSs and MBSs. Although the consequences of  $\theta$  seem to be similar in the trivial and topological phases, the presence of MBSs in the topological phase makes the JDs susceptible to their properties such as the inherent Majorana nonlocality, which we address in the next section.

## V. CRITICAL CURRENTS AND JOSEPHSON DIODE'S EFFICIENCIES

To further understand the non-reciprocal Josephson transport and characterize the JD effect, here we examine the critical currents  $I_c^\pm$  associated to  $I(\phi)$  and also inspect the degree of non-reciprocity that such critical currents exhibit. As already mentioned before, non-reciprocal critical currents signal the emergence of the JD effect. Below we address the critical currents and diode efficiencies in JJs studied in the previous section unless otherwise stated.

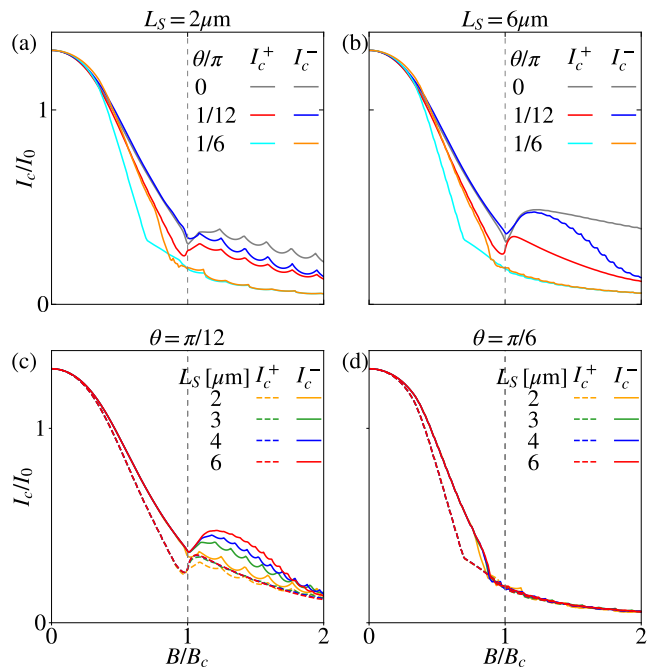


FIG. 5. (a,b) Critical currents  $I_c^\pm$  as a function of the Zeeman field amplitude  $B$  for distinct values of  $\theta$ , and at  $L_S = 2 \mu\text{m}$  and  $L_S = 6 \mu\text{m}$ . (c,d) The same as in (a,b) but at fixed  $\theta = \pi/12$  and  $\theta = \pi/6$  for different  $L_S$ . Parameters:  $L_N = 20 \text{ nm}$ ,  $\tau = 1$ ,  $I_0 = e\Delta/2\hbar$ , while the rest of parameters are the same as in Fig. 2.

### A. Non-reciprocal critical currents

We begin by inspecting the critical currents across transparent short JJs as a function of the Zeeman field amplitude, which is presented in Fig. 5(a,b) for short and long superconducting regions at distinct values of  $\theta$ . Fig. 5(c,d) shows the Zeeman dependent critical currents at two fixed  $\theta$  for different  $L_S$ . At  $\theta = 0$ , the critical currents  $I_c^+$  and  $I_c^-$  coincide since the low-energy phase-dependent spectrum is symmetric and  $I(\phi)$  develops a regular behavior already reported before, see gray curves in Fig. 5(a,b). As  $B$  increases within  $B < B_c$ , the critical currents  $I_c^\pm$  at  $\theta = 0$  reduce and, at  $B = B_c$  when  $\Delta_1 = 0$ , they exhibit a kink-like feature whose finite value arises due to the phase dependence of the low-energy spectrum. In the topological phase  $B > B_c$ , the critical currents develop an oscillatory profile as  $B$  increases, which originate due to the zero-energy splitting of the four MBSs at  $\phi = \pi$  [Fig. 2(d)]. The oscillations in the Zeeman dependent critical currents are then washed out when the superconducting regions are longer than twice the Majorana localization length, see gray curve in Fig. 5(b); this situation also enhances the critical current since for a superconductor of infinite length, the critical current is due to  $\Delta_2$ . Hence, the critical currents trace the gap closing and reopening of  $\Delta_1$  as well as the emergence of MBSs protected by  $\Delta_2$ .

When  $\theta \neq 0$ , we find that the critical currents can be distinct, namely,  $I_c^+ \neq I_c^-$ , thus reflecting non-reciprocal Josephson transport, see Fig. 5(a,b). Despite the effect of  $\theta$ , both critical currents still exhibit features of the gap closing and reopening at  $B = B_c$  and also develop the oscillations of MBSs in the topological phase which reduce for long superconductors. An interesting feature to remark, and which might affect the identification of the topological phase, is that  $I_c^+$  tends to decrease faster with  $B$  in the trivial phase for certain  $\theta$ , originating a large difference between  $I_c^+$  and  $I_c^-$ , see e. g., red (cyan) and blue (orange) curves in Fig. 5(a). The finite values of  $\theta$  also soften the critical current oscillations due to MBSs [Fig. 5(a)] and tend to reduce the critical current values in the topological phase, see Fig. 5(a,b). The reduction of the critical current in the topological phase is associated to the decrease (or even vanishing) of the topological gap separating MBSs from the quasicontinuum, which becomes more evident when the superconductor length  $L_S$  is very long as then the topological gap is given by the bulk gap  $\Delta_2$  [Fig. 5(b)].

Further insights on the length of the superconductors is obtained from Fig. 5(c,d), where the critical currents are shown for distinct  $L_S$  at fixed  $\theta$ . For certain  $\theta \neq 0$  with an already present non-reciprocity, increasing the length  $L_S$  enhances the difference between  $I_c^+$  and  $I_c^-$  in the topological phase but leaves unchanged the critical currents in the trivial phase, see Fig. 5(c) for  $\theta = \pi/12$ ; in Fig. 5(d), the response of the critical currents to variations in  $L_S$  is negligible mainly because MBSs are almost dispersionless with  $\phi$  [Fig. 2(f)]. The dependence on the length of the superconductors can only be attributed to the spatial nonlocality of MBSs since they are located at the ends of the superconductors. Additionally, the period of the critical current oscillations increases with  $L_S$ , which is attributed to the growing number of Majorana zero-energy crossings in the topological regime [115]. The non-reciprocity in the critical currents can thus sense the emergence of MBSs, while MBSs are able to enhance the diode behavior. Taking into account the above discussion, the found non-reciprocity in the critical currents  $I_c^\pm$  at  $\theta \neq 0$  demonstrates the emergence of the JD effect with ABSs and MBSs, and its controllability by the amplitude of the Zeeman field  $B$ .

## B. Efficiency of the Josephson diode effect

To further understand the emergence of the JDs, in this part we characterize the amount of non-reciprocity of the critical currents by the quality factor  $\eta = (I_c^+ - I_c^-)/(I_c^+ + I_c^-)$ . Thus, the quality factor  $\eta$  measures the efficiency of the JD and  $\eta \neq 0$  signals the emergence of the JD effect;  $\eta$  is sometimes referred to as efficiency as well. In Fig. 6(a,b) we present the quality factor  $\eta$  as a function of the Zeeman field amplitude  $B$  and  $\theta$  in transparent short JJs with short and long superconductors. The first feature we notice is that  $\eta$  acquires finite values when both

$B$  and  $\theta$  are nonzero, reflecting the key role of the Zeeman field  $B_y$  parallel to the SO axis, see blue and red regions in Fig. 6(a,b). As  $B$  increases, the diode's efficiency first acquires nonzero values  $\eta \neq 0$  in the trivial phase and, as  $B$  drives the system into the topological phase,  $\eta$  remains finite but with a profile that is tied to the presence of MBSs. In fact, in the topological phase,  $\eta$  as a function of  $B$  has an oscillatory profile that depends on  $L_S$  and reveals the presence of MBSs, see Fig. 6(a,b). An interesting consequence of MBSs in the topological phase is that when MBSs become truly zero modes, e. g., in JJs with very long superconductors, the diode's efficiencies get enhanced entirely due to the spatial Majorana nonlocality; in the trivial phase,  $\eta$  is not altered by  $L_S$  since there are no nonlocal quasiparticles. The enhancement of  $\eta$  by means of Majorana nonlocality is also seen in Fig. 6(c), where we show  $\eta$  versus  $B$  for distinct values of  $L_S$  at  $\theta = \pi/12$ ; in this regime, MBSs still disperse with  $\phi$  [Fig. 2(e)] and the bulk gap  $\Delta_2$  vanishes deep in the topological phase [Fig. 1(d)]. At  $\theta = \pi/6$ , MBSs are dispersionless almost coexisting with the quasicontinuum [Fig. 2(f)] and no effect of the Majorana nonlocality on  $\eta$  is observed [Fig. 6(d)]; here the bulk gap  $\Delta_2$  vanishes before  $B_c$ . Thus, when  $\Delta_2$  vanishes in the topological regime (as in the case of  $\theta = \pi/12$ ), the diode efficiency increases with superconductor length. Conversely, when  $\Delta_2$  vanishes in the trivial regime (as in the case of  $\theta = \pi/6$ ),  $\eta$  remains unchanged regardless of  $L_S$ .

Another feature we highlight in Fig. 6(a,b) is that  $\eta$  exhibits positive and negative values, which, surprisingly, occur in both the trivial and topological phases; hence, the reversal of diode's polarity occurs with ABSs and MBSs in the trivial and topological phases, respectively. For transparent JJs with short superconductors, the maximum value of  $\eta$  occurs below  $B_c$  for all  $\theta$ , with the position of this maximum shifting away from  $B = B_c$  as  $\theta$  increases. Notably, positive efficiencies  $\eta > 0$  in the trivial regime appear only when  $\Delta_2$  vanishes in this regime, which we demonstrate by showing that the locus of  $\eta = 0$  follows the curve where  $\Delta_2 = 0$ , as indicated by the magenta dotted line in Fig. 6(a,b). The curve where the diode's polarity changes sign in the trivial phase does not depend on  $L_S$ , which unveils that the junction does not host quasiparticles that are nonlocal in space affecting  $\eta$  and that reversing its polarity is very likely a bulk effect. In the topological phase, the situation is more intriguing because the change in diode's polarity does not follow  $\Delta_2 = 0$ . In short and long superconductors, positive efficiencies appear at low but finite values of  $\theta$ , while negative efficiencies can happen at much higher  $\theta$ , in both cases revealing the Majorana oscillations. In contrast to the trivial regime, the efficiencies acquire larger positive values in the topological phase when the superconductors are longer, an indicator that MBSs are playing an important role [Fig. 6(b)]. It is worth noting that the large positive values of  $\eta$  in the topological phase of JJs with long superconductors develop a sudden decrease at  $\theta$  where  $\Delta_2 = 0$  but the signatures of Majorana oscilla-

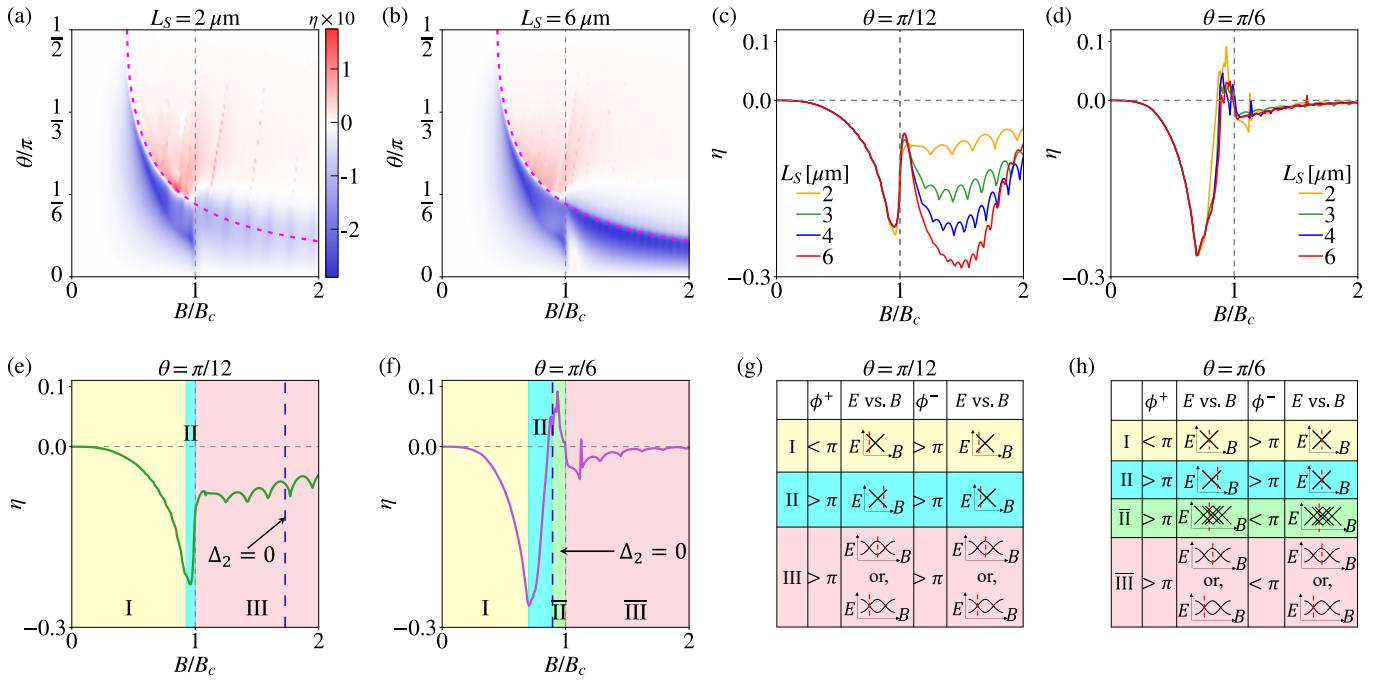


FIG. 6. (a,b) Quality factor  $\eta$  of the JDs as a function of the Zeeman field amplitude  $B$  and  $\theta$  in JJs with short ( $L_S = 2 \mu\text{m}$ ) and long ( $L_S = 4 \mu\text{m}$ ) superconductors. The vertical dashed gray line marks the topological phase transition  $B = B_c$  where the bulk gap  $\Delta_1$  vanishes, while the dotted magenta curve corresponds to the vanishing of the bulk gap  $\Delta_2$ . (c,d) Quality factor  $\eta$  versus  $B$  at two values of  $\theta$  in (a,b), including their evolution as the length of the superconductors  $L_S$  gets longer. (e,f)  $\eta$  versus  $B$  from (a) at  $\theta = \pi/12$  and  $\theta = \pi/6$  for  $L_S = 2 \mu\text{m}$ , indicating distinct regions that correspond to the behavior of  $\eta$ . The vertical dashed blue lines indicate the points where the bulk gap  $\Delta_2 = 0$ . (g,h) Table that shows the phases  $\phi_{\pm}$  at which  $I_c^{\pm}$  occur in each region of (e,f), accompanied with a sketch of their respective energy versus  $B$  around zero energy. In each  $E$  vs.  $B$  of (g,h), the red dashed line indicates the value of  $B$  at which  $\eta$  is evaluated. Parameters:  $L_N = 20 \text{ nm}$ ,  $\tau = 1$ ,  $I_0 = e\Delta/2\hbar$ , while the rest of parameters are the same as in Fig. 2.

tions remain.

Further insights on the behavior of  $\eta$  and its relation to the low-energy spectrum is shown in Fig. 6(e,f) at  $L_S = 2 \mu\text{m}$ , where the Zeeman evolution of  $\eta$  for  $\theta = \pi/12$  and  $\theta = \pi/6$  is divided into distinct regions according to the phases  $\phi_{\pm}$  at which the critical currents  $I_c^{\pm}$  in the current-phase curves  $I(\phi)$  occur, see Fig. 6(g,h). It should be noted that  $\phi_+$  and  $\phi_-$  evolve continuously with variations in  $B$  and  $\theta$ . Thus, we divide the efficiency curve for  $\theta = \pi/6$  and  $\theta = \pi/12$  into four and three distinct regions, respectively, see Fig. 6(e,f); we remind that for  $\theta = \pi/6$  the bulk gap  $\Delta_2$  vanishes just below  $B_c$ , while for  $\theta = \pi/12$  it vanishes deep in the topological phase. The energy versus  $B$  shown in Fig. 6(g,h) is obtained at the phases  $\phi_{\pm}$  corresponding to  $I_c^{\pm}$ . In the case of  $\theta = \pi/12$ ,  $\phi_+$  and  $\phi_-$  emerge before the appearance of zero-energy ABSs, see region I depicted in yellow in Fig. 6(e,g). As  $B$  increases,  $\phi_+$  shifts beyond  $\pi$  and  $I_c^+$  appears away from the ABSs but  $\phi_-$  remains at the  $B$  position of the zero-energy ABS, see region II in Fig. 6(e,g); in the topological phase with MBSs,  $\phi_{\pm}$  remains above  $\pi$ , see region III in Fig. 6(e,g). For  $\theta = \pi/6$  in Fig. 6(f,h), the efficiency curve consists of four regions due to the closing of  $\Delta_2$  in the trivial regime. In the trivial phase,  $\phi_{\pm}$  in regions I and II closely resembles that observed for  $\theta = \pi/12$ ,

but the additional region,  $\bar{\text{II}}$  is slightly distinct. In this region, the diode's polarity is reversed. Near to the topological phase transition but above  $B$  where  $\Delta_2 = 0$ ,  $\phi_-$  remains below  $\pi$ , and multiple zero-energy levels appear in the  $E$  vs.  $B$  spectrum due to the vanishing of  $\Delta_2$  at the onset of this region, see region  $\bar{\text{II}}$  in Fig. 6(f,h). The region corresponding to the topological phase, that is, region  $\bar{\text{III}}$  is different from the corresponding region III at  $\theta = \pi/12$ ,  $\phi_{+(-)}$  at  $\theta = \pi/6$  are above (below)  $\pi$ , see Fig. 6(f,h). Consequently, in transparent JJs, the JD effect due to distinct critical currents ( $I_c^{\pm}$ ) may arise either in the presence or absence of trivial ABSs or topological MBSs.

### C. Majorana-only Josephson diode effect controlled by normal transmission

All of the preceding results, showing the emergence of JDs in the trivial and topological phases with ABSs and MBSs, respectively, pertain to a transparent JJ based on the model given by Eq. (2). Motivated by the fact that critical currents due to ABSs and MBSs have a distinct dependence on the normal transmission  $T_N$ , here we explore how the JD effect responds to variations of such



a transmission as  $B$  transitions from the trivial to the topological phases. As noted in Section II, the parameter  $\tau$  between nearest-neighbor sites in the superconducting and normal regions controls the normal transmission: by reducing  $\tau$ , the tunneling regime  $T_N \ll 1$  is achieved at  $\tau \approx 0.5$  [115], albeit, at  $\tau = 0.6$ , the junction already exhibits  $T_N \ll 1$ ; in the transparent regime,  $\tau = 1$  corresponds to  $T_N = 1$ . That being said, in Fig. 7(a-d) we present the critical currents  $I_c^\pm$  and quality factor  $\eta$  as a function of  $B$  for two representative values of  $\theta$  at  $L_S = 2 \mu\text{m}$ . In Fig. 7(e,f), we show  $\eta$  as a function of  $B$  and  $\theta$  for two distinct values of  $L_S$  in the tunneling regime. As  $\tau$  decreases in the trivial phase  $B < B_c$ , the critical currents  $I_c^\pm$  get reduced until they become negligible in the tunneling regime at  $\tau \approx 0.5$ . The kink-like feature near  $B = B_c$  found for transparent JJs [Fig. 5] changes into a step-like profile as  $\tau$  reduces, producing a sudden reentrant critical currents at the topological phase transition in the tunneling regime even when such critical currents vanish below  $B_c$ , see Fig. 7(a) for  $\theta = \pi/12$ . Interestingly, this re-entrant effect arises due to the distinct contribution to the critical currents coming either from ABSs in the trivial phase or MBSs in the topological phase. In fact, the critical current mediated by MBSs at  $\theta = 0$  scales as  $\sim \sqrt{T_N}$ , while the critical currents due to ABSs are proportional to  $\sim T_N$ , leading to vanishing critical currents in the trivial phase in the tunneling regime. We have verified that this critical current behavior persists at small but nonzero values of  $\tau$ , thus explaining the vanishing of critical current due to ABSs in the tunneling regime in Fig. 7(a,b). Furthermore, the oscillations of the Majorana-driven critical currents for  $B > B_c$  reduce their periodicity as  $\tau$  is reduced, with a doubled periodicity in the tunneling regime in comparison to the transparent regime, see Fig. 7(a,b). This period doubling is a direct result of the four MBSs being decoupled in the tunneling regime, such that two MBSs in each superconductor still oscillate with the same period when  $B$  increases. A similar behavior is observed for  $\theta = \pi/6$ , albeit the oscillatory  $I_c^\pm$  in the  $B > B_c$  region is weaker due to the almost dispersionless energy spectrum with  $\phi$  [Fig. 2(f)]. Therefore, in the tunnelling regime,  $I_c^\pm$  diminishes everywhere except in the topological phase where MBSs appear, originating Majorana-driven non-reciprocal critical currents and hence a Majorana-only JD effect.

When it comes to the efficiency of the non-reciprocal critical currents in the tunneling regime,  $\eta$  exhibits vanishing values in the trivial phase for  $\tau \ll 1$  for any  $\theta$ , see Fig. 7(c,d). In the  $B > B_c$  regime,  $\eta$  shows the oscillatory behavior with doubled periodicity in the tunneling regime irrespective of the value of  $\theta$ . It is fair to say that, despite having a Majorana-only JD effect, its resulting efficiency is low due to a decreased difference between  $I_c^+$  and  $I_c^-$  in the tunneling regime. Further insights on  $\eta$  are obtained from Fig. 7(e,f), where we show  $\eta$  as a function of both  $B$  and  $\theta$  in the tunneling regime and for short and long superconductors. In this case, the diode's efficiency

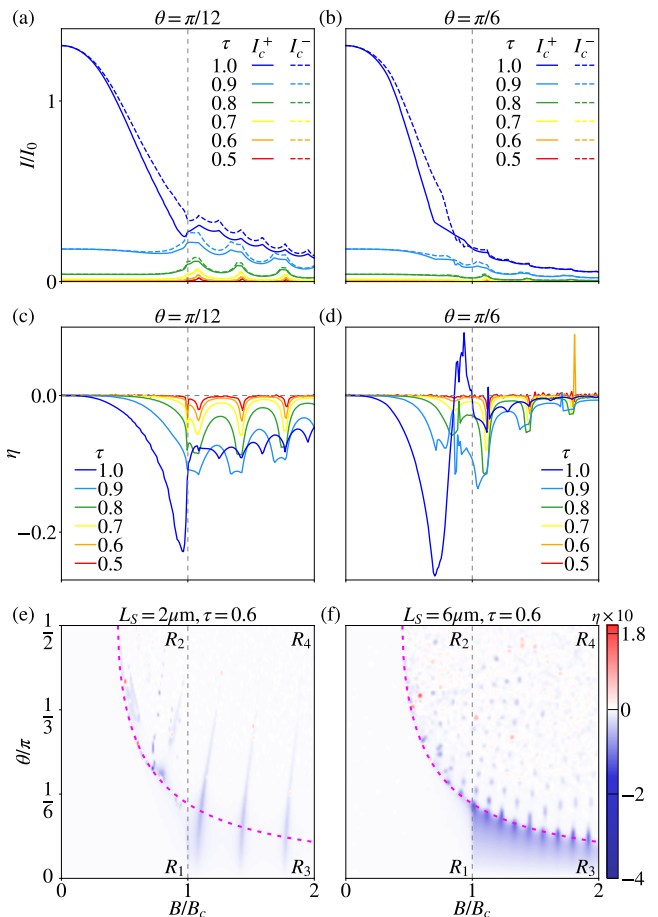


FIG. 7. (a,b) Critical currents and quality factors (c,d) as a function of  $B$  at finite  $\theta$  and different values of  $\tau$ . The solid and dashed curves in (a,b) correspond to  $I_c^+$  and  $I_c^-$ , respectively, while the vertical dashed gray line marks  $B = B_c$ . (e,f) The quality factor  $\eta$  as a function of both  $B$  and  $\theta$  at  $\tau = 0.6$  in JJs with short and long superconductors. The magenta dotted curve represents the vanishing of  $\Delta_2$ , while the gray dashed line signifies the vanishing of  $\Delta_1$ . Here,  $R_{1,2}$  ( $R_{3,4}$ ) regions have  $\Delta_2 \geq 0$  respectively, and lies in the trivial (topological) regime. Parameters: the same as in Fig. 6.

is found to vanish  $\eta = 0$  in the trivial phase  $B < B_c$  only when  $\Delta_2 > 0$ , see region  $R_1$  below the magenta dotted curve in Fig. 7(e,f) marking  $\Delta_2 = 0$ ; see also Fig. 1(d).

Below such magenta curve, where no JD appears in the trivial phase, a sizeable diode's efficiency is confirmed revealing the period doubling effect due to MBSs. Above such magenta curve in the trivial phase where  $\Delta_2 < 0$ , however, a finite JD effect appears, which can be understood as a nontrivial effect of  $\theta$  on the transparency dependence of the critical currents discussed before; here,  $\Delta_2$  vanishes in the trivial phase, a bunch of ABSs around zero energy affect the critical currents that then promote a nonzero JD efficiency. Nevertheless, below  $\Delta_2 = 0$  no JD effect appears in the trivial phase. As a result, in the tunneling regime, one can eliminate the effect of ABSs and JDs can operate only with MBSs in the topological

phase.

## VI. CONCLUSIONS

We investigated the emergence of the Josephson diode effect in Josephson junctions that can be realized using superconductor-semiconductor hybrids under an homogeneous magnetic field. We have shown that the component of the Zeeman field parallel to the spin-orbit axis originates a phase-dependent energy spectrum that is asymmetric as a function of the phase difference in the trivial and topological phases of transparent Josephson junctions with Andreev and Majorana bound states, respectively. We have then demonstrated that this asymmetry is the key ingredient for realizing current-phase curves with unequal positive and negative critical currents, which, signal non-reciprocal transport that characterizes the Josephson diode effect. We have further showed that the Josephson diodes can be controlled by the Zeeman field magnitude, where the diode's efficiency traces the gap closing and reopening as well as the oscillations of Majorana bound states in the topological phase. As a result, while the Josephson diode effect occurs in the presence of Andreev or Majorana bound states, it develops an intriguing response only in the topological phase due to the intrinsic spatial Majorana nonlocality that even enhances the Josephson diode's efficiency. Furthermore, we have discovered that, by reducing the normal transmission also reduces the diode's efficiency in the trivial phase and a Josephson diode effect only appears in the topological phase with Majorana bound states. We have also verified that our findings remain robust at finite but low temperatures. Our work can therefore be useful for understanding the emergence of Josephson diodes under the presence of Andreev and Majorana bound states in semiconductor-superconductor hybrids as well as for identifying the topological phase.

## ACKNOWLEDGMENTS

We thank L. Arrachea, J.-F. Liu, and W. Xu for valuable discussions. S. M. and J. C. acknowledge financial support from the Göran Gustafsson Foundation (Grant No. 2216), the Swedish Research Council (Vetenskapsrådet Grant No. 2021-04121) and the Carl Trygger's Foundation (Grant No. 22: 2093). P.-H. Fu is supported by the National Natural Science Foundation of China (Grant No. 12174077). The computations were enabled by resources provided by the National Academic Infrastructure for Supercomputing in Sweden (NAISS), partially funded by the Swedish Research Council through Grant Agreement No. 2022-06725.

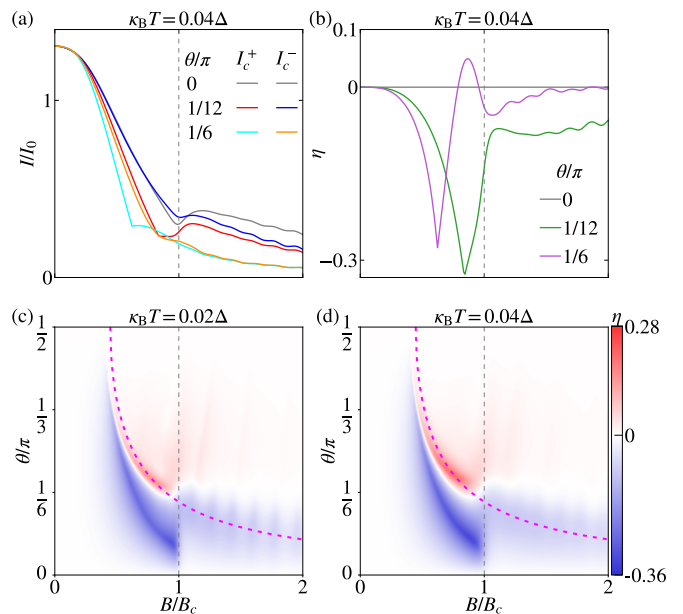


FIG. 8. (a) The critical currents and (b) the efficiencies are shown for  $k_B T = 0.04\Delta$  as a function  $B/B_c$ . Panels [(c) and (d)] displays the efficiency as a function of  $B$  and  $\theta$ , where the magenta dotted line represents the  $\Delta_2 = 0$  curve. The vertical dashed line in each panel represents the vanishing of bulk gap,  $\Delta_1 = 0$ .

## Appendix A: Effect of temperature on the efficiency of the Josephson diodes

In the main text, we have discussed efficiency  $\eta$  both for a transparent JJ and a JJ in the tunnelling regime. In the first case, we have observed the finite  $\eta$  when the system hosts ABSs and MBSs. In contrast, in the tunneling regime,  $\eta$  exhibits a strong dependence on MBSs alone. Moreover, in this regime,  $\eta$  shows a re-entrant behavior at  $B = B_c$  and an oscillatory pattern with double periodicity in the nontrivial phase. However, the effect of a small but finite temperature differs from that in the tunneling regime. Although a slight increase in temperature suppresses the MBS-driven oscillations of efficiency in the topological phase, but the efficiency remains robust. We have verified that current phase curve follows a nonreciprocal behavior in presence of such small temperature. We only show the critical currents and the efficiency below.

To provide a complete picture of the effect of a small temperature, we present the variation of both the critical currents  $I_c^\pm$  and the efficiency  $\eta$  with the Zeeman field  $B$  in Fig. 8(a,b) for three representative values of  $\theta$ . For the calculation, we set a small temperature  $\kappa_B T = 0.04\Delta$ , ensuring it remains below the superconducting order parameter. Furthermore, we present  $\eta$  as a function of both  $B$  and  $\theta$  in Fig. 8(c,d) for two different temperatures  $\kappa_B T = 0.02\Delta$  and  $\kappa_B T = 0.04\Delta$ . For  $\theta = 0$ , the identical critical currents,  $I_c^\pm$ , exhibit features [see Fig. 8(a)] similar to those observed at zero temperature in the  $B < B_c$

region. At  $B = B_c$ , a kink-like feature appears. In the  $B > B_c$  region, an oscillatory pattern emerges but with a suppressed amplitude. For  $\theta \neq 0$ , the distinct critical currents,  $I_c^+$  and  $I_c^-$ , display a larger difference in the trivial regime compared to their zero-temperature counterparts, see the red (cyan) and blue (yellow) curves for  $\theta = \pi/12$  ( $\pi/6$ ) in Fig. 8(a). However, in the topological regime, the Majorana-driven oscillatory pattern is now suppressed, similar to the case of  $\theta = 0$ . Thus, the small temperature primarily smooths out oscillations and suppresses features related to MBSs, while enhancing the difference between critical currents in the trivial regime.

When it comes to the efficiency at the non-zero temperature,  $\eta$  exhibits enhanced values in the trivial regime as compared to that for  $\kappa_B T = 0$ , see the purple and green curves in Fig. 8(b). This enhancement arises from the increased difference between  $I_c^+$  and  $I_c^-$  in the trivial

regime. In the topological phase,  $\eta$  retains its oscillatory pattern but with a reduced amplitude. Moreover, the presence of a nonzero temperature smooths the curve, making the peaks and dips less pronounced. Further insights on  $\eta$  is obtained from Fig. 8(c,d), where we illustrate its dependence on both  $B$  and  $\theta$  for different values of  $\kappa_B T$ . In the trivial regime, both positive and negative  $\eta$  exhibit increased magnitudes. Additionally, as  $\theta$  increases, the maximum  $\eta$  shifts away from  $B = B_c$ . Notably, the locus of  $\eta = 0$  (represented by the thin white region sandwiched between the red and blue regions in the trivial regime) moves away from the  $\Delta_2 = 0$  curve. Importantly, in the topological phase, the amplitude of the MBS-driven oscillatory pattern diminishes as the temperature increases. Therefore, the non-vanishing nature of the efficiency suggests that it remains robust against a small but finite temperature.

- 
- [1] B. Josephson, Possible new effects in superconductive tunnelling, *Phys. Lett.* **1**, 251 (1962).
- [2] K. K. Likharev, Superconducting weak links, *Rev. Mod. Phys.* **51**, 101 (1979).
- [3] Y. Makhlin, G. Schön, and A. Shnirman, Quantum-state engineering with Josephson-junction devices, *Rev. Mod. Phys.* **73**, 357 (2001).
- [4] A. A. Golubov, M. Y. Kupriyanov, and E. Il'ichev, The current-phase relation in Josephson junctions, *Rev. Mod. Phys.* **76**, 411 (2004).
- [5] A. I. Buzdin, Proximity effects in superconductor-ferromagnet heterostructures, *Rev. Mod. Phys.* **77**, 935 (2005).
- [6] F. S. Bergeret, A. F. Volkov, and K. B. Efetov, Odd triplet superconductivity and related phenomena in superconductor-ferromagnet structures, *Rev. Mod. Phys.* **77**, 1321 (2005).
- [7] N. O. Birge and N. Satchell, Ferromagnetic materials for Josephson  $\pi$  junctions, *APL Mater.* **12** (2024).
- [8] M. Amundsen, J. Linder, J. W. A. Robinson, I. Žutić, and N. Banerjee, Colloquium: Spin-orbit effects in superconducting hybrid structures, *Rev. Mod. Phys.* **96**, 021003 (2024).
- [9] A. Acín, I. Bloch, H. Buhrman, T. Calarco, C. Eichler, J. Eisert, D. Esteve, N. Gisin, S. J. Glaser, F. Jelezko, *et al.*, The quantum technologies roadmap: a European community view, *New J. Phys.* **20**, 080201 (2018).
- [10] Y. Fukaya, B. Lu, K. Yada, Y. Tanaka, and J. Cayao, Superconducting phenomena in systems with unconventional magnets, [arXiv:2502.15400](https://arxiv.org/abs/2502.15400) (2025).
- [11] I. Kulik and A. Omel'Yanchuk, Contribution to the microscopic theory of the Josephson effect in superconducting bridges, *JETP Lett.* **21**, 216 (1975).
- [12] A. Furusaki and M. Tsukada, Dc Josephson effect and Andreev reflection, *Solid State Commun.* **78**, 299 (1991).
- [13] A. Furusaki, H. Takayanagi, and M. Tsukada, Josephson effect of the superconducting quantum point contact, *Phys. Rev. B* **45**, 10563 (1992).
- [14] C. Beenakker, Three "universal" mesoscopic Josephson effects, in *Transport phenomena in mesoscopic systems: Proceedings of the 14th Taniguchi symposium, Shima, Japan, November 10-14, 1991*, Vol. 109 (Springer-Verlag, 1992) p. 235.
- [15] A. Furusaki, Josephson current carried by Andreev levels in superconducting quantum point contacts, *Superlattices Microstruct.* **25**, 809 (1999).
- [16] S. Kashiwaya and Y. Tanaka, Tunnelling effects on surface bound states in unconventional superconductors, *Rep. Prog. Phys.* **63**, 1641 (2000).
- [17] Y. Asano, Direct-current Josephson effect in SNS junctions of anisotropic superconductors, *Phys. Rev. B* **64**, 224515 (2001).
- [18] Y. Asano, Y. Tanaka, and S. Kashiwaya, Anomalous Josephson effect in  $p$ -wave dirty junctions, *Phys. Rev. Lett.* **96**, 097007 (2006).
- [19] J. Sauls, Andreev bound states and their signatures, *Philos. Trans. Royal Soc. A* **376**, 20180140 (2018).
- [20] T. Mizushima and K. Machida, Multifaceted properties of Andreev bound states: interplay of symmetry and topology, *Philos. Trans. R. Soc. A* **376**, 20150355 (2018).
- [21] M. H. Devoret and J. M. Martinis, Implementing qubits with superconducting integrated circuits, *Quant. Info. Proc.* , 163 (2005).
- [22] G. Wendin and V. Shumeiko, Quantum bits with Josephson junctions, *Low Temp. Phys.* **33**, 724 (2007).
- [23] J. Clarke and F. K. Wilhelm, Superconducting quantum bits, *Nature* **453**, 1031 (2008).
- [24] M. Kjaergaard, M. E. Schwartz, J. Braumüller, P. Krantz, J. I.-J. Wang, S. Gustavsson, and W. D. Oliver, Superconducting qubits: Current state of play, *Annu. Rev. Condens. Matter Phys.* **11**, 369 (2020).
- [25] R. Aguado, A perspective on semiconductor-based superconducting qubits, *Appl. Phys. Lett.* **117**, 240501 (2020).
- [26] R. Aguado and L. P. Kouwenhoven, Majorana qubits for topological quantum computing, *Phys. Today* **73**, 44 (2020).
- [27] G. Burkard, Hybrid superconductor-semiconductor systems for quantum technology, *Appl. Phys. Lett.* **116** (2020).
- [28] I. Siddiqi, Engineering high-coherence superconducting

- qubits, *Nat. Rev. Mater.* **6**, 875 (2021).
- [29] M. Eschrig, Spin-polarized supercurrents for spintronics, *Phys. Today* **64**, 43 (2011).
- [30] J. Linder and J. W. Robinson, Superconducting spintronics, *Nat. Phys.* **11**, 307 (2015).
- [31] M. Eschrig, Spin-polarized supercurrents for spintronics: a review of current progress, *Rep. Prog. Phys.* **78**, 104501 (2015).
- [32] G. Yang, C. Ciccarelli, and J. W. Robinson, Boosting spintronics with superconductivity, *APL Mater.* **9** (2021).
- [33] A. Mel'nikov, S. V. Mironov, A. V. Samokhvalov, and A. I. Buzdin, Superconducting spintronics: state of the art and prospects, *Uspekhi Fiz. Nauk* **192**, 1339 (2022).
- [34] R. Cai, I. Žutić, and W. Han, Superconductor/ferromagnet heterostructures: A platform for superconducting spintronics and quantum computation, *Adv. Quantum Technol.* **6**, 2200080 (2023).
- [35] R. Jaklevic, J. Lambe, A. Silver, and J. Mercereau, Quantum interference effects in Josephson tunneling, *Phys. Rev. Lett.* **12**, 159 (1964).
- [36] A. Silver and J. Zimmerman, Quantum states and transitions in weakly connected superconducting rings, *Phys. Rev.* **157**, 317 (1967).
- [37] R. Kleiner, D. Koelle, F. Ludwig, and J. Clarke, Superconducting quantum interference devices: State of the art and applications, *Proc. IEEE* **92**, 1534 (2004).
- [38] J. Clarke and A. I. Braginski, *The SQUID handbook: fundamentals and technology of SQUIDS and SQUID systems* (John Wiley & Sons, 2006).
- [39] C. Granata and A. Vettoliere, Nano superconducting quantum interference device: A powerful tool for nanoscale investigations, *Phys. Rep.* **614**, 1 (2016).
- [40] A. Serebinski, A. W. Draelos, E. G. Arnault, M.-T. Wei, H. Li, T. Fleming, K. Watanabe, T. Taniguchi, F. Amet, and G. Finkelstein, Quantum Hall-based superconducting interference device, *Sci. Adv.* **5**, eaaw8693 (2019).
- [41] J. Hu, C. Wu, and X. Dai, Proposed design of a Josephson diode, *Phys. Rev. Lett.* **99**, 067004 (2007).
- [42] F. Dolcini, M. Houzet, and J. S. Meyer, Topological Josephson  $\phi_0$  junctions, *Phys. Rev. B* **92**, 035428 (2015).
- [43] K. N. Nesterov, M. Houzet, and J. S. Meyer, Anomalous Josephson effect in semiconducting nanowires as a signature of the topologically nontrivial phase, *Phys. Rev. B* **93**, 174502 (2016).
- [44] K. Misaki and N. Nagaosa, Theory of the nonreciprocal Josephson effect, *Phys. Rev. B* **103**, 245302 (2021).
- [45] Y. Tanaka, B. Lu, and N. Nagaosa, Theory of giant diode effect in  $d$ -wave superconductor junctions on the surface of a topological insulator, *Phys. Rev. B* **106**, 214524 (2022).
- [46] M. Davydova, S. Prembabu, and L. Fu, Universal Josephson diode effect, *Sci. Adv.* **8**, eabo0309 (2022).
- [47] M. Nadeem, M. S. Fuhrer, and X. Wang, The superconducting diode effect, *Nat. Rev. Phys.* **5**, 558 (2023).
- [48] A. Maiani, K. Flensberg, M. Leijnse, C. Schrade, S. Vaitiekėnas, and R. Seoane Souto, Non-sinusoidal current-phase relations in semiconductor–superconductor–ferromagnetic insulator devices, *Phys. Rev. B* **107**, 245415 (2023).
- [49] R. S. Souto, M. Leijnse, and C. Schrade, Josephson diode effect in supercurrent interferometers, *Phys. Rev. Lett.* **129**, 267702 (2022).
- [50] A. Costa, J. Fabian, and D. Kochan, Microscopic study of the Josephson supercurrent diode effect in Josephson junctions based on two-dimensional electron gas, *Phys. Rev. B* **108**, 054522 (2023).
- [51] D. Debnath and P. Dutta, Gate-tunable Josephson diode effect in Rashba spin-orbit coupled quantum dot junctions, *Phys. Rev. B* **109**, 174511 (2024).
- [52] B. Scharf, D. Kochan, and A. Matos-Abiague, Superconducting diode effect in quantum spin Hall insulator based Josephson junctions, *Phys. Rev. B* **110**, 134511 (2024).
- [53] J. L. Huamani Correa and M. P. Nowak, Theory of universal diode effect in three-terminal Josephson junctions, *SciPost Phys.* **17**, 037 (2024).
- [54] Q.-K. Shen and Y. Zhang, Josephson diodes induced by the loop current states, [arXiv:2409.09938](https://arxiv.org/abs/2409.09938) (2024).
- [55] A. Soori, Josephson diode effect in one-dimensional quantum wires connected to superconductors with mixed singlet-triplet pairing, *J. Condens. Matter Phys.* **37**, 10LT02 (2025).
- [56] E. Nikodem, J. Schluck, M. Geier, M. Papaj, H. F. Legg, J. Feng, M. Bagchi, L. Fu, and Y. Ando, Large tunable Josephson diode effect in a side-contacted topological-insulator-nanowire junction, [arXiv:2412.16569](https://arxiv.org/abs/2412.16569) (2024).
- [57] D. Debnath and P. Dutta, Field-free Josephson diode effect in interacting chiral quantum dot junctions, [arXiv:2411.18325](https://arxiv.org/abs/2411.18325) (2024).
- [58] G. P. Mazur, N. van Loo, D. van Driel, J.-Y. Wang, L. P. Kouwenhoven, G. Badawy, S. Gazibegovic, and E. Bakkers, Gate-tunable Josephson diode, *Phys. Rev. Appl.* **22**, 054034 (2024).
- [59] H. Wu, Y. Wang, Y. Xu, P. K. Sivakumar, C. Pasco, U. Filippozzi, S. S. Parkin, Y.-J. Zeng, T. McQueen, and M. N. Ali, The field-free Josephson diode in a van der Waals heterostructure, *Nature* **604**, 653 (2022).
- [60] C. Baumgartner, L. Fuchs, A. Costa, J. Picó-Cortés, S. Reinhardt, S. Gronin, G. C. Gardner, T. Lindemann, M. J. Manfra, P. F. Junior, *et al.*, Effect of Rashba and Dresselhaus spin-orbit coupling on supercurrent rectification and magnetochiral anisotropy of ballistic Josephson junctions, *J. Condens. Matter Phys.* **34**, 154005 (2022).
- [61] C. Baumgartner, L. Fuchs, A. Costa, S. Reinhardt, S. Gronin, G. C. Gardner, T. Lindemann, M. J. Manfra, P. E. Faria Junior, D. Kochan, J. Fabian, N. Paradiso, and C. Strunk, Supercurrent rectification and magnetochiral effects in symmetric Josephson junctions, *Nat. Nanotech.* **17**, 39 (2022).
- [62] B. Pal, A. Chakraborty, P. K. Sivakumar, M. Davydova, A. K. Gopi, A. K. Pandeya, J. A. Krieger, Y. Zhang, M. Date, S. Ju, *et al.*, Josephson diode effect from Cooper pair momentum in a topological semimetal, *Nat. Phys.* **18**, 1228 (2022).
- [63] A. Kudriashov, X. Zhou, R. Hovhannisyan, A. Frolov, L. Elesin, Y. Wang, E. Zharkova, T. Taniguchi, K. Watanabe, L. Yashina, *et al.*, Non-reciprocal current-phase relation and superconducting diode effect in topological-insulator-based Josephson junctions, [arXiv:2502.08527](https://arxiv.org/abs/2502.08527) (2025).
- [64] J.-X. Hu, Z.-T. Sun, Y.-M. Xie, and K. T. Law, Josephson diode effect induced by valley polarization in twisted bilayer graphene, *Phys. Rev. Lett.* **130**, 266003 (2023).
- [65] Y. Zhang, Y. Gu, P. Li, J. Hu, and K. Jiang, General theory of Josephson diodes, *Phys. Rev. X* **12**, 041013 (2022).

- [66] Z. Ding, D. Wang, M. Li, Y. Tao, and J. Wang, Spin-resolved and charge Josephson diode effects in  $\alpha - T_3$  lattice junctions, *Phys. Rev. B* **110**, 155405 (2024).
- [67] B. Turini, S. Salimian, M. Carrega, A. Iorio, E. Strambini, F. Giazotto, V. Zannier, L. Sorba, and S. Heun, Josephson diode effect in high-mobility insb nanoflags, *Nano Lett.* **22**, 8502 (2022).
- [68] Q. Cheng, Y. Mao, and Q.-F. Sun, Field-free Josephson diode effect in altermagnet/normal metal/altermagnet junctions, *Phys. Rev. B* **110**, 014518 (2024).
- [69] S. Banerjee and M. S. Scheurer, Altermagnetic superconducting diode effect, *Phys. Rev. B* **110**, 024503 (2024).
- [70] P. Kotetes, M. Roig, and B. M. Andersen, Nonreciprocal equilibrium  $4\pi$ -periodic Josephson effect from poor man's Majorana zero modes, [arXiv:2409.13027](https://arxiv.org/abs/2409.13027) (2024).
- [71] M. Trahms, L. Melischek, J. F. Steiner, B. Mahendru, I. Tamir, N. Bogdanoff, O. Peters, G. Reecht, C. B. Winkelmann, F. von Oppen, and K. J. Franke, Diode effect in Josephson junctions with a single magnetic atom, *Nature* **615**, 628 (2023).
- [72] S. Ilić and F. S. Bergeret, Theory of the supercurrent diode effect in Rashba superconductors with arbitrary disorder, *Phys. Rev. Lett.* **128**, 177001 (2022).
- [73] Z. Liu, L. Huang, and J. Wang, Josephson diode effect in topological superconductors, *Phys. Rev. B* **110**, 014519 (2024).
- [74] R. Seoane Souto, M. Leijnse, C. Schrade, M. Valentini, G. Katsaros, and J. Danon, Tuning the Josephson diode response with an ac current, *Phys. Rev. Res.* **6**, L022002 (2024).
- [75] S. Fracassi, S. Traverso, N. Traverso Ziani, M. Carrega, S. Heun, and M. Sasseti, Anomalous supercurrent and diode effect in locally perturbed topological Josephson junctions, *Appl. Phys. Lett.* **124** (2024).
- [76] H. F. Legg, K. Laubscher, D. Loss, and J. Klinovaja, Parity-protected superconducting diode effect in topological Josephson junctions, *Phys. Rev. B* **108**, 214520 (2023).
- [77] T. Karabassov, I. V. Bobkova, A. A. Golubov, and A. S. Vasenko, Hybrid helical state and superconducting diode effect in superconductor/ferromagnet/topological insulator heterostructures, *Phys. Rev. B* **106**, 224509 (2022).
- [78] P.-H. Fu, Y. Xu, S. A. Yang, C. H. Lee, Y. S. Ang, and J.-F. Liu, Field-effect Josephson diode via asymmetric spin-momentum locking states, *Phys. Rev. Appl.* **21**, 054057 (2024).
- [79] B. Lu, S. Ikegaya, P. Buset, Y. Tanaka, and N. Nagaosa, Tunable Josephson diode effect on the surface of topological insulators, *Phys. Rev. Lett.* **131**, 096001 (2023).
- [80] J. J. Cuzzo, W. Pan, J. Shabani, and E. Rossi, Microwave-tunable diode effect in asymmetric SQUIDs with topological Josephson junctions, *Phys. Rev. Res.* **6**, 023011 (2024).
- [81] J. Cayao, N. Nagaosa, and Y. Tanaka, Enhancing the Josephson diode effect with Majorana bound states, *Phys. Rev. B* **109**, L081405 (2024).
- [82] J. S. Meyer and M. Houzet, Josephson diode effect in a ballistic single-channel nanowire, *Appl. Phys. Lett.* **125** (2024).
- [83] M. Valentini, O. Sagi, L. Baghumyan, T. de Gijssel, J. Jung, S. Calcaterra, A. Ballabio, J. A. Servin, K. Aggarwal, M. Janik, T. Adletzberger, R. S. Souto, M. Leijnse, J. Danon, C. Schrade, E. Bakkers, D. Chrastina, G. Isella, and G. Katsaros, Parity-conserving cooper-pair transport and ideal superconducting diode in planar germanium, [arXiv:2306.07109](https://arxiv.org/abs/2306.07109) (2023).
- [84] Y. Hou, F. Nichele, H. Chi, A. Lodesani, Y. Wu, M. F. Ritter, D. Z. Haxell, M. Davydova, S. Ilić, O. Glezakou-Elbert, A. Varambally, F. S. Bergeret, A. Kamra, L. Fu, P. A. Lee, and J. S. Moodera, Ubiquitous superconducting diode effect in superconductor thin films, *Phys. Rev. Lett.* **131**, 027001 (2023).
- [85] A. A. Aligia, D. Pérez Daroca, and L. Arrachea, Tomography of zero-energy end modes in topological superconducting wires, *Phys. Rev. Lett.* **125**, 256801 (2020).
- [86] N. Lotfizadeh, W. F. Schiela, B. Pekerten, P. Yu, B. H. Elfeky, W. M. Strickland, A. Matos-Abiague, and J. Shabani, Superconducting diode effect sign change in epitaxial Al-InAs Josephson junctions, *Commun. Phys.* **7**, 120 (2024).
- [87] A. I. Braginski, Superconductor electronics: Status and outlook, *J. Supercond. Nov. Magn.* **32**, 23 (2019).
- [88] J. C. Gallop, *SQUIDS, the Josephson effects and superconducting electronics* (CRC press, 2017).
- [89] S. Anders, M. Blamire, F.-I. Buchholz, D.-G. Crété, R. Cristiano, P. Febvre, L. Fritzsche, A. Herr, E. Il'ichev, J. Kohlmann, *et al.*, European roadmap on superconductive electronics—status and perspectives, *Physica C: Superconductivity* **470**, 2079 (2010).
- [90] S. Hoshino, R. Wakatsuki, K. Hamamoto, and N. Nagaosa, Nonreciprocal charge transport in two-dimensional noncentrosymmetric superconductors, *Phys. Rev. B* **98**, 054510 (2018).
- [91] R. Wakatsuki, Y. Saito, S. Hoshino, Y. M. Itahashi, T. Ideue, M. Ezawa, Y. Iwasa, and N. Nagaosa, Nonreciprocal charge transport in noncentrosymmetric superconductors, *Sci. Adv.* **3**, e1602390 (2017).
- [92] N. Nagaosa and Y. Yanase, Nonreciprocal transport and optical phenomena in quantum materials, *Annu. Rev. Condens. Matter Phys.* **15**, 63 (2024).
- [93] Y. Tokura and N. Nagaosa, Nonreciprocal responses from non-centrosymmetric quantum materials, *Nat. Commun.* **9**, 3740 (2018).
- [94] S. M. Sze and M.-K. Lee, *Semiconductor Devices: Physics and Technology* (Wiley, Hoboken, NJ, 2016).
- [95] I. Mehdi, J. V. Siles, C. Lee, and E. Schlecht, THz diode technology: Status, prospects, and applications, *Proc. IEEE* **105**, 990 (2017).
- [96] J. Semple, D. G. Georgiadou, G. Wyatt-Moon, G. Gelinck, and T. D. Anthopoulos, Flexible diodes for radio frequency (RF) electronics: A materials perspective, *Semicond. Sci. Technol.* **32**, 123002 (2017).
- [97] L. A. Coldren, S. W. Corzine, and M. L. Mashanovitch, *Diode Lasers and Photonic Integrated Circuits* (John Wiley & Sons, 2012).
- [98] N. F. Yuan and L. Fu, Supercurrent diode effect and finite-momentum superconductors, *Proc. Natl. Acad. Sci. U. S. A.* **119**, e2119548119 (2022).
- [99] A. Daido, Y. Ikeda, and Y. Yanase, Intrinsic superconducting diode effect, *Phys. Rev. Lett.* **128**, 037001 (2022).
- [100] J. J. He, Y. Tanaka, and N. Nagaosa, A phenomenological theory of superconductor diodes, *New J. Phys.* **24**, 053014 (2022).
- [101] F. Ando, Y. Miyasaka, T. Li, J. Ishizuka, T. Arakawa,

- Y. Shiota, T. Moriyama, Y. Yanase, and T. Ono, Observation of superconducting diode effect, *Nature* **584**, 373 (2020).
- [102] M. Sato and S. Fujimoto, Majorana fermions and topology in superconductors, *J. Phys. Soc. Jpn.* **85**, 072001 (2016).
- [103] R. Aguado, Majorana quasiparticles in condensed matter, *Riv. Nuovo Cimento* **40**, 523 (2017).
- [104] M. Sato and Y. Ando, Topological superconductors: A review, *Rep. Prog. Phys.* **80**, 076501 (2017).
- [105] R. M. Lutchyn, E. P. Bakkers, L. P. Kouwenhoven, P. Krogstrup, C. M. Marcus, and Y. Oreg, Majorana zero modes in superconductor–semiconductor heterostructures, *Nat. Rev. Mater.* **3**, 52 (2018).
- [106] E. Prada, P. San-Jose, M. W. de Moor, A. Geresdi, E. J. Lee, J. Klinovaja, D. Loss, J. Nygård, R. Aguado, and L. P. Kouwenhoven, From Andreev to Majorana bound states in hybrid superconductor–semiconductor nanowires, *Nat. Rev. Phys.* **2**, 575 (2020).
- [107] J. Cayao, C. Triola, and A. M. Black-Schaffer, Odd-frequency superconducting pairing in one-dimensional systems, *Eur. Phys. J. Special Topics* **229**, 545 (2020).
- [108] K. Flensberg, F. von Oppen, and A. Stern, Engineered platforms for topological superconductivity and Majorana zero modes, *Nat. Rev. Mater.* **6**, 944 (2021).
- [109] S. M. Frolov, M. J. Manfra, and J. D. Sau, Topological superconductivity in hybrid devices, *Nat. Phys.* **16**, 718 (2020).
- [110] P. Marra, Majorana nanowires for topological quantum computation, *J. Appl. Phys.* **132**, 231101 (2022).
- [111] Y. Tanaka, S. Tamura, and J. Cayao, Theory of Majorana zero modes in unconventional superconductors, *Prog. Theor. Exp. Phys.* **2024**, 08C105 (2024).
- [112] P. San-Jose, E. Prada, and R. Aguado, ac Josephson effect in finite-length nanowire junctions with Majorana modes, *Phys. Rev. Lett.* **108**, 257001 (2012).
- [113] P. San-Jose, J. Cayao, E. Prada, and R. Aguado, Multiple Andreev reflection and critical current in topological superconducting nanowire junctions, *New J. Phys.* **15**, 075019 (2013).
- [114] J. Cayao, E. Prada, P. San-Jose, and R. Aguado, SNS junctions in nanowires with spin-orbit coupling: Role of confinement and helicity on the subgap spectrum, *Phys. Rev. B* **91**, 024514 (2015).
- [115] J. Cayao, P. San-Jose, A. M. Black-Schaffer, R. Aguado, and E. Prada, Majorana splitting from critical currents in Josephson junctions, *Phys. Rev. B* **96**, 205425 (2017).
- [116] Y. Peng, F. Pientka, E. Berg, Y. Oreg, and F. von Oppen, Signatures of topological Josephson junctions, *Phys. Rev. B* **94**, 085409 (2016).
- [117] J. Cayao, A. M. Black-Schaffer, E. Prada, and R. Aguado, Andreev spectrum and supercurrents in nanowire-based SNS junctions containing Majorana bound states, *Beilstein J. Nanotechnol.* **9**, 1339 (2018).
- [118] J. Cayao and A. M. Black-Schaffer, Distinguishing trivial and topological zero-energy states in long nanowire junctions, *Phys. Rev. B* **104**, L020501 (2021).
- [119] B. Pekerten, J. D. Pakizer, B. Hawn, and A. Matos-Abiague, Anisotropic topological superconductivity in Josephson junctions, *Phys. Rev. B* **105**, 054504 (2022).
- [120] L. Baldo, L. G. D. Da Silva, A. M. Black-Schaffer, and J. Cayao, Zero-frequency supercurrent susceptibility signatures of trivial and topological zero-energy states in nanowire junctions, *Supercond. Sci. Technol.* **36**, 034003 (2023).
- [121] O. A. Awoga, J. Cayao, and A. M. Black-Schaffer, Supercurrent detection of topologically trivial zero-energy states in nanowire junctions, *Phys. Rev. Lett.* **123**, 117001 (2019).
- [122] M. Hays, G. de Lange, K. Serniak, D. J. van Woerkom, D. Bouman, P. Krogstrup, J. Nygård, A. Geresdi, and M. H. Devoret, Direct microwave measurement of Andreev-bound-state dynamics in a semiconductor-nanowire Josephson junction, *Phys. Rev. Lett.* **121**, 047001 (2018).
- [123] L. Tosi, C. Metzger, M. F. Goffman, C. Urbina, H. Pothier, S. Park, A. L. Yeyati, J. Nygård, and P. Krogstrup, Spin-orbit splitting of Andreev states revealed by microwave spectroscopy, *Phys. Rev. X* **9**, 011010 (2019).
- [124] H. Ren, F. Pientka, S. Hart, A. T. Pierce, M. Kosowsky, L. Lunczer, R. Schlereth, B. Scharf, E. M. Hankiewicz, L. W. Molenkamp, B. I. Halperin, and A. Yacoby, Topological superconductivity in a phase-controlled Josephson junction, *Nature* **569**, 93 (2019).
- [125] F. Nichele, E. Portolés, A. Fornieri, A. M. Whiticar, A. C. C. Drachmann, S. Gronin, T. Wang, G. C. Gardner, C. Thomas, A. T. Hatke, M. J. Manfra, and C. M. Marcus, Relating Andreev bound states and supercurrents in hybrid Josephson junctions, *Phys. Rev. Lett.* **124**, 226801 (2020).
- [126] M. Sato, Y. Takahashi, and S. Fujimoto, Non-abelian topological order in *s*-wave superfluids of ultracold fermionic atoms, *Phys. Rev. Lett.* **103**, 020401 (2009).
- [127] M. Sato, Y. Takahashi, and S. Fujimoto, Non-Abelian topological orders and Majorana fermions in spin-singlet superconductors, *Phys. Rev. B* **82**, 134521 (2010).
- [128] R. M. Lutchyn, J. D. Sau, and S. Das Sarma, Majorana fermions and a topological phase transition in semiconductor-superconductor heterostructures, *Phys. Rev. Lett.* **105**, 077001 (2010).
- [129] Y. Oreg, G. Refael, and F. von Oppen, Helical liquids and Majorana bound states in quantum wires, *Phys. Rev. Lett.* **105**, 177002 (2010).
- [130] J. Cayao, *Hybrid superconductor-semiconductor nanowire junctions as useful platforms to study Majorana bound states*, Phd thesis, Autonomous University of Madrid (UAM), Madrid, Spain (2016), see Chapter.
- [131] V. K. Vimal and J. Cayao, Entanglement measures of Majorana bound states, *Phys. Rev. B* **110**, 224510 (2024).
- [132] E. Ahmed, S. Tamura, Y. Tanaka, and J. Cayao, Odd-frequency pairing due to Majorana and trivial Andreev bound states, [arXiv: 2412.14439](https://arxiv.org/abs/2412.14439) (2024).